Supplementary Information

Long-wavelength near-infrared in chromium-activated $LiZnNbO_4$ spinel crystal and valence-converting emission enhancement via Lanthanum ion heterotopic doping

Wen Song[1], Kaiwen Zhang[1], Xiaoyi Dong[1], Liang Xu[1], Yongjin Li[1,2*], Rui Hu[3*], Zhaoyi Yin[1,2], Zhengwen Yang[1,2], Jianbei Qiu[1,2], Zhiguo Song[1,2*]

[1]Faculty of Material Science and Engineering, Kunming University of Science and Technology, Kunming 650093, PR China
[2]Key Lab. of Advanced Materials of Yunnan Province, Kunming 650093, PR China
[3]Collage of Chemistry and Chemical Engineering, China West Normal University, Nanchong 637000, PR China

Correspondence: liyongjin@kust.edu.cn (Y. Li), hr2022@cwnu.edu.cn (R. Hu), songzg@kust.edu.cn (Z. Song).

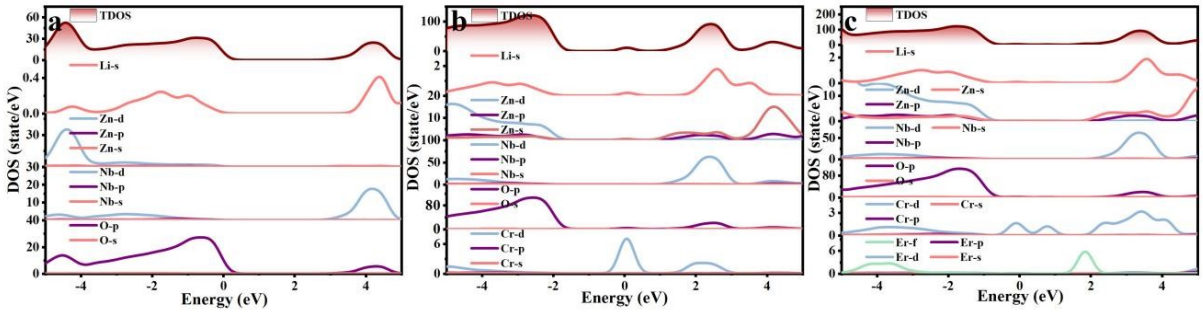

Figure S1. a)、(b) and c) are total and partial density of states of $LiZnNbO_4$ host、$LiZnNbO_4:Cr^{3+}$ and $LiZnNbO_4:Cr^{3+},Er^{3+}$.

Fig. S1 displays the total and partial density of states (DOS), revealing that the primary influence on the maximum valence band (VBM) of LZNO is from O 2p orbitals, while the minimum conduction band (CBM) is mainly influenced by Nb 4d orbitals. Cr^{3+} doping results in the overall energy band shifting towards lower energy directions, and the Cr 3d states are situated in the center of the band gap, divided into filled t_{2g} states and empty e_g states. Clearly, the introduction of Er^{3+} creates an impurity level at the bottom of the conduction band and a new t_{2g} state of Cr^{3+} at the top of the valence band. This results in a reduction in the energy gap between the highest valence states and the ground states of Cr^{3+}.

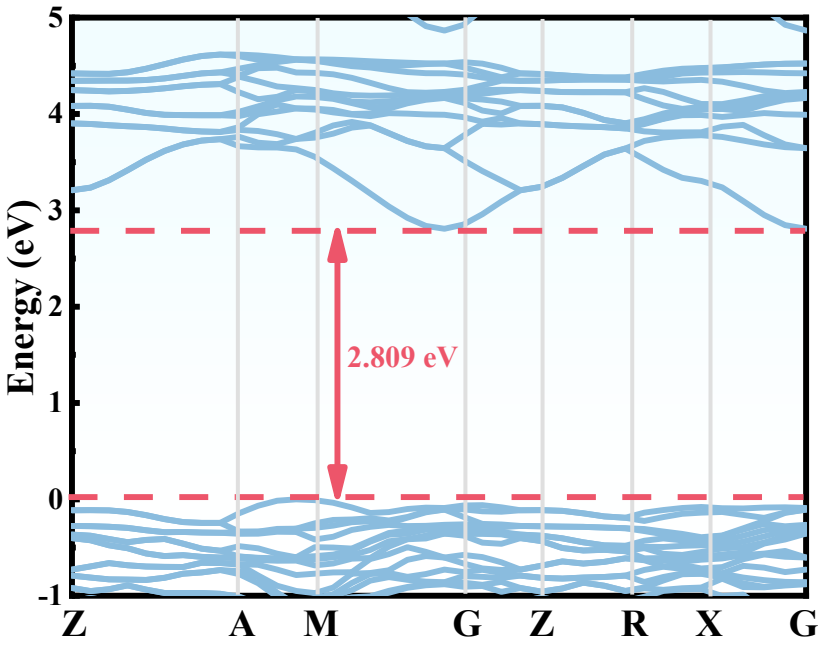

Figure S2. Calculated of electronic band structure of $LiZnNbO_4$ host.

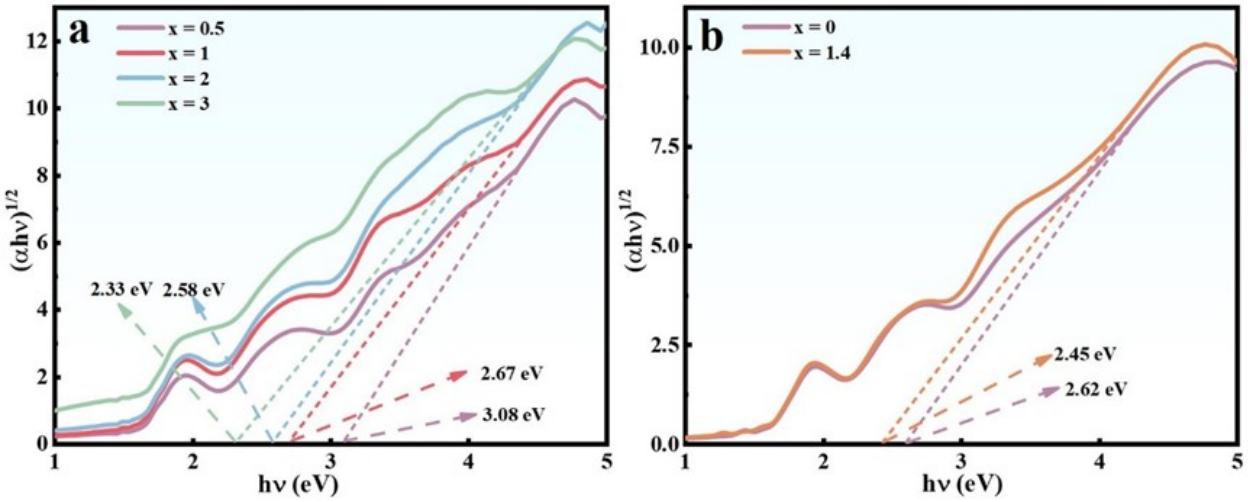

Figure S3. a) and (b) are absorption spectra of LZNO:x%Cr^{3+} (x = 0.5, 1, 2 and 3) and LZNO:1%Cr^{3+},x%Er^{3+} (x = 0 and 1.4) calculated by the Kubelka-Munk equation.

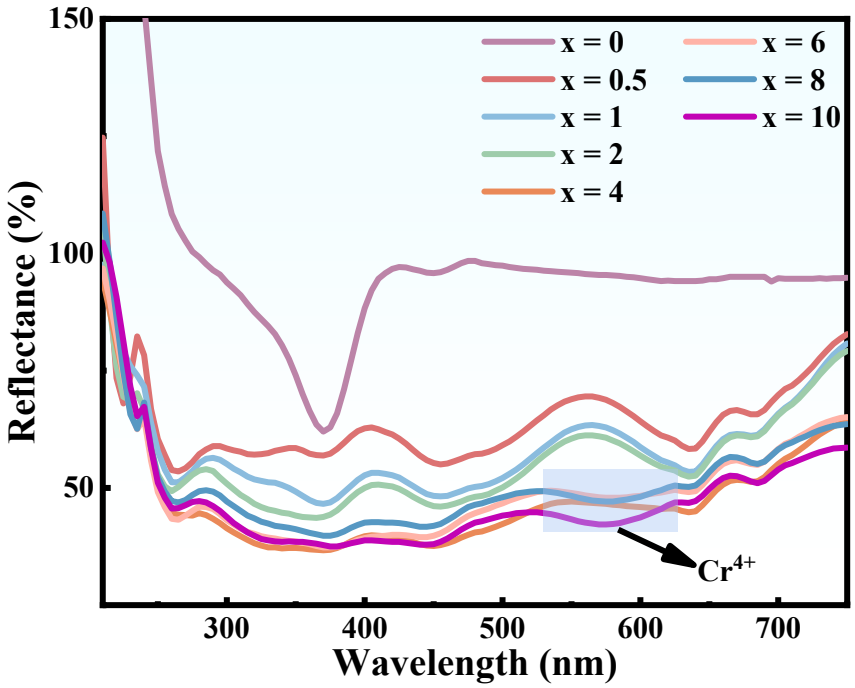

Figure S4. Diffuse reflectance spectra of LZNO:x%Cr^{3+} (x = 0-10).

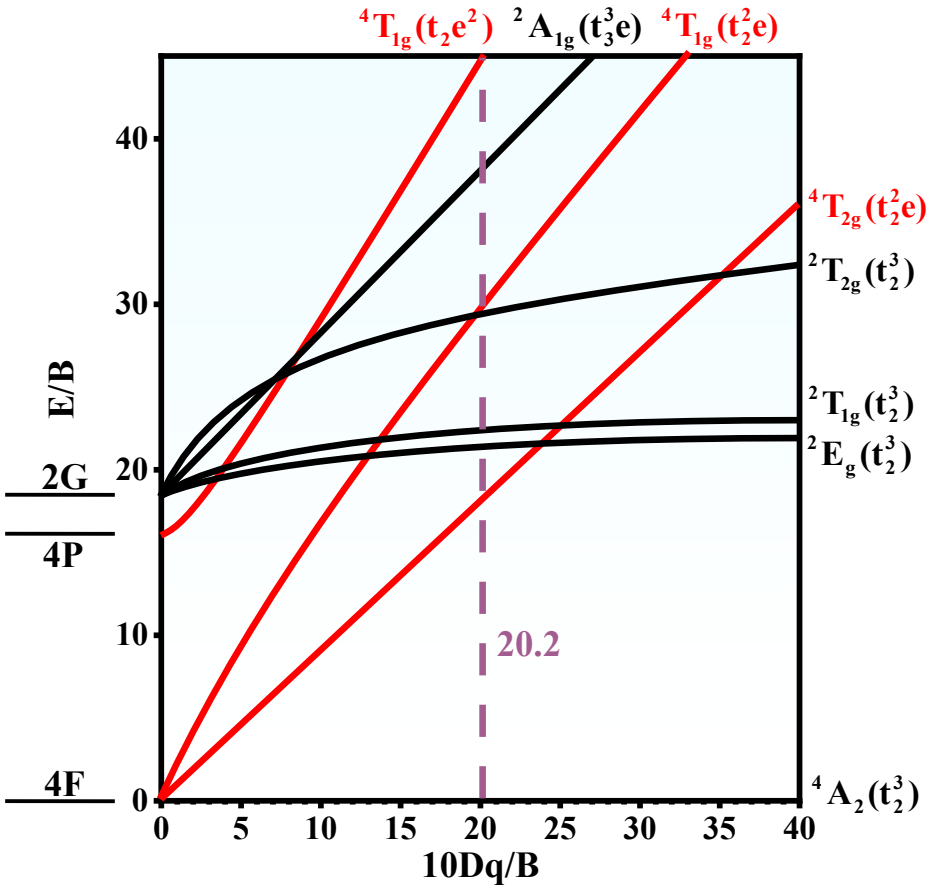

Figure S5. Tanabe-Sugano diagram for Cr^{3+} in an octahedral site.

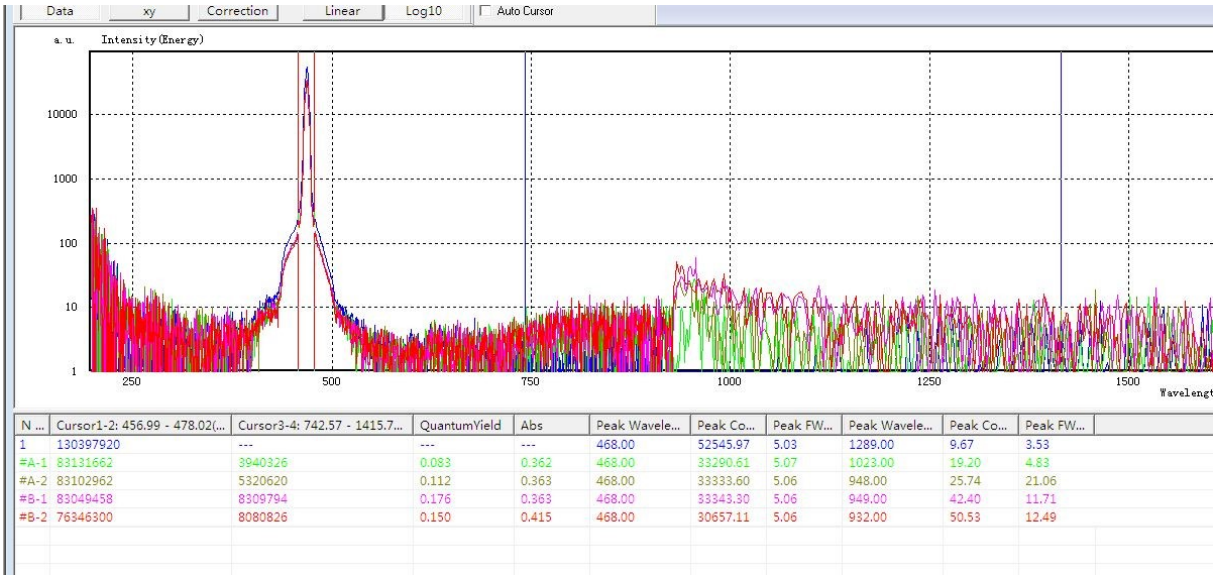

N ...	Cursor1-2: 456.99 - 478.02(...	Cursor3-4: 742.57 - 1415.7...	QuantumYield	Abs	Peak Wavele...	Peak Co...	Peak FW...	Peak Wavele...	Peak Co...	Peak FW...
1	130397920	---	---	---	468.00	52545.97	5.03	1289.00	9.67	3.53
#A-1	83131662	3940326	0.083	0.362	468.00	33290.61	5.07	1023.00	19.20	4.83
#A-2	83102962	5320620	0.112	0.363	468.00	33333.60	5.06	948.00	25.74	21.06
#B-1	83049458	8309794	0.176	0.363	468.00	33343.30	5.06	949.00	42.40	11.71
#B-2	76346300	8080826	0.150	0.415	468.00	30657.11	5.06	932.00	50.53	12.49

Figure S6. Absolute photoluminescence quantum yield (PLQY) of LZNO:0.01Cr^{3+} and LZNO:0.01Cr^{3+},0.014Er^{3+}.

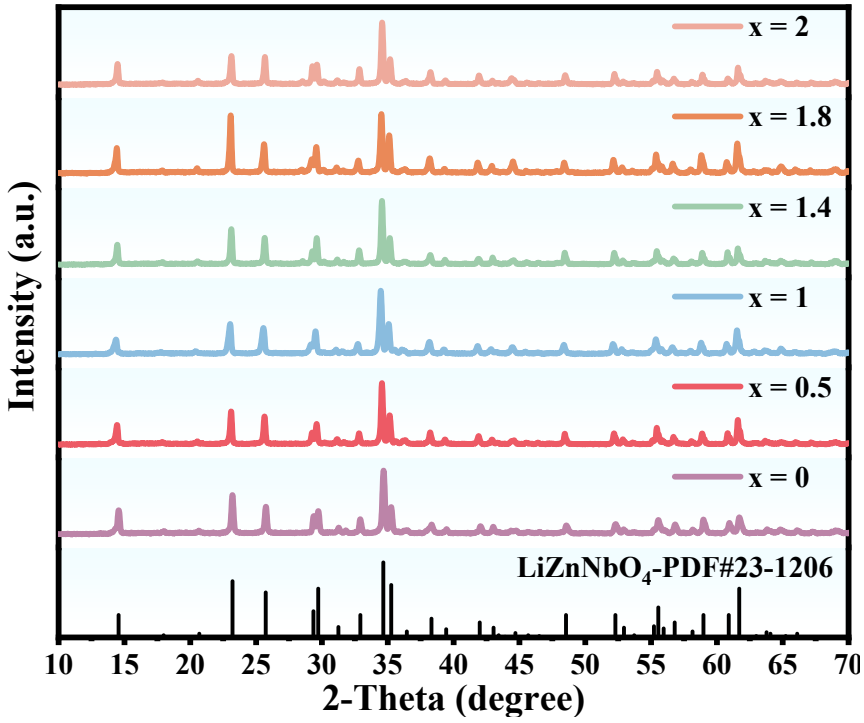

Figure S7. XRD patterns of LZNO:1%Cr^{3+},x%Er^{3+} (x = 0-10) at room temperature.

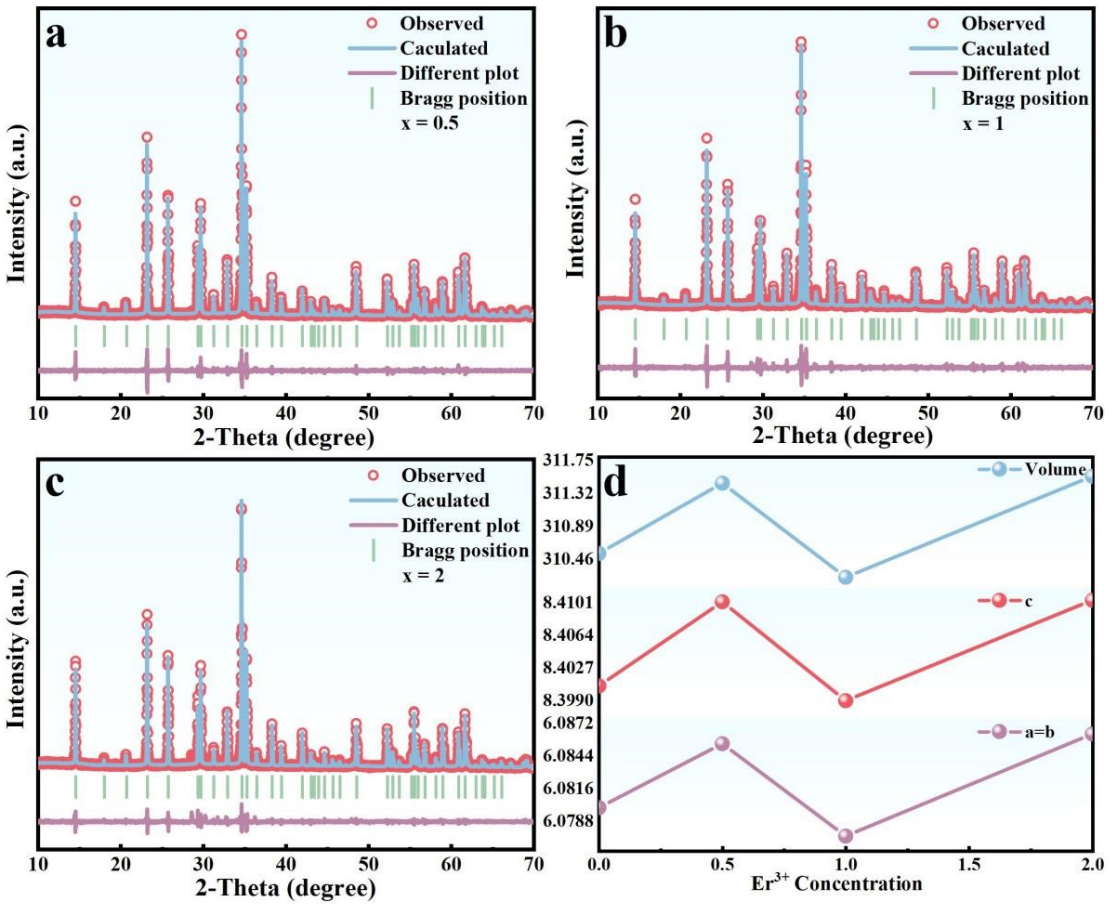

Figure S8. Rietveld refinement profiles of (a) LZNO:1%Cr^{3+},0.5%Er^{3+}, (b) LZNO:1%Cr^{3+},1%Er^{3+}, (c) LZNO:1%Cr^{3+},2%Er^{3+}. (d) Changes in the cell parameters (a, b, c) and unit cell volume in LZNO:1%Cr^{3+},x%Er^{3+} with x increasing.

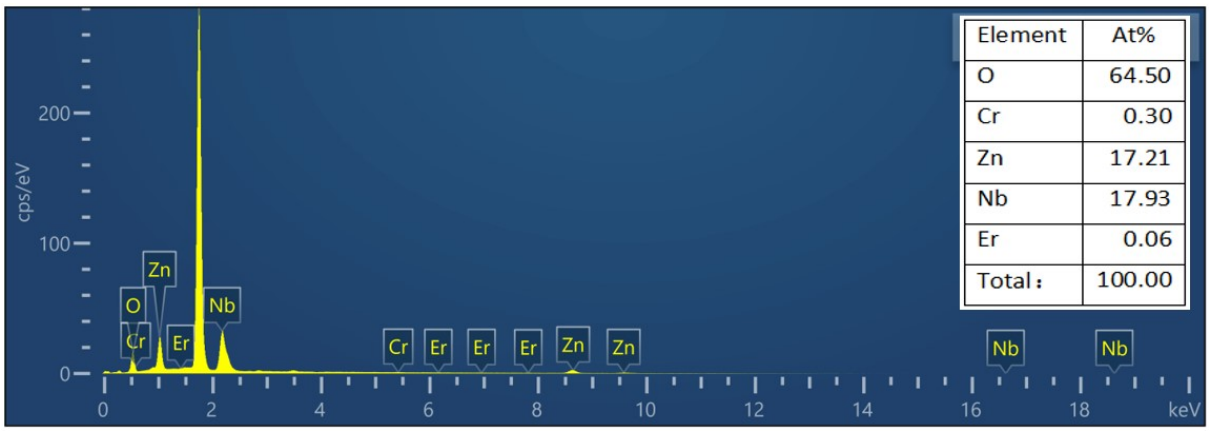

Figure S9. EDS spectrum of LZNO:0.01Cr^{3+},0.014Er^{3+} sample.

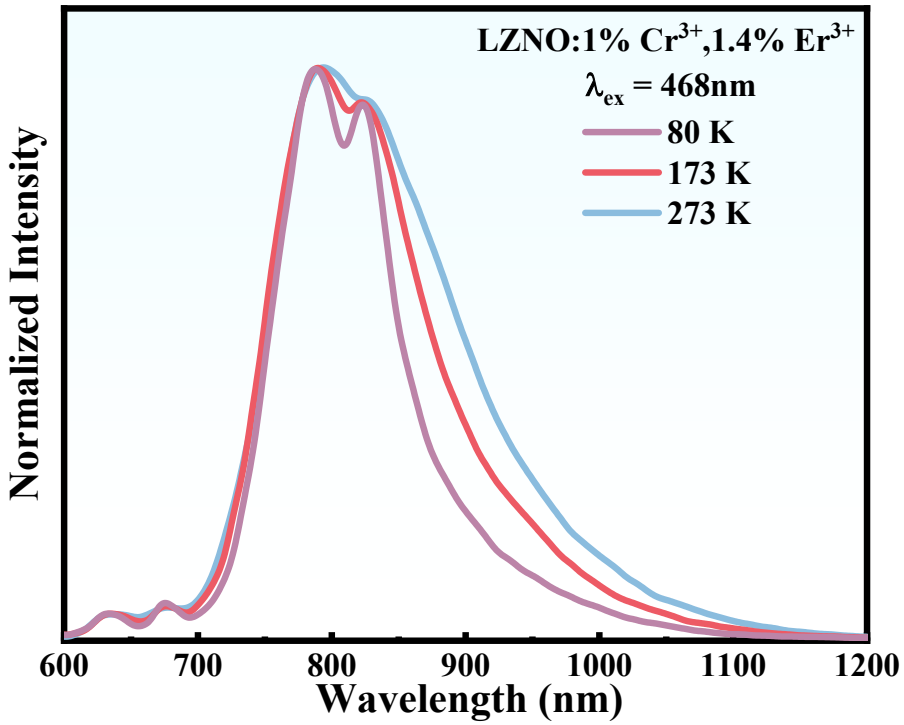

Figure S10. Emission spectra of LZNO:1%Cr^{3+},1.4%Er^{3+} measured at 273, 173 and 80 K.

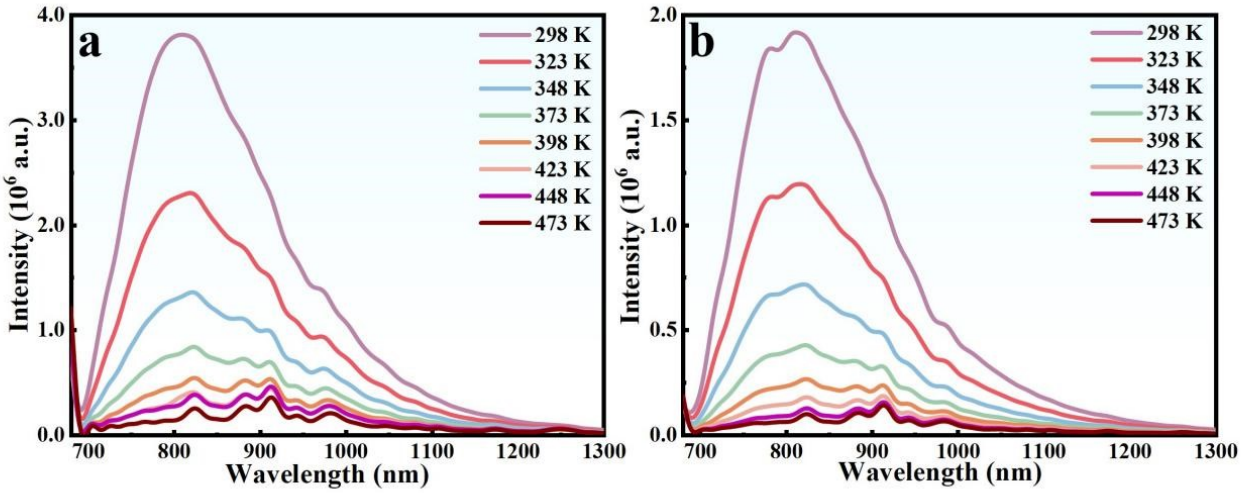

Figure S11. a) and (b) are temperature-dependent emission spectra were tested from 298 to 473 K under 468 nm excitation of LZNO:0.01Cr^{3+} and LZNO:0.01Cr^{3+},0.014Er^{3+}, respectively.

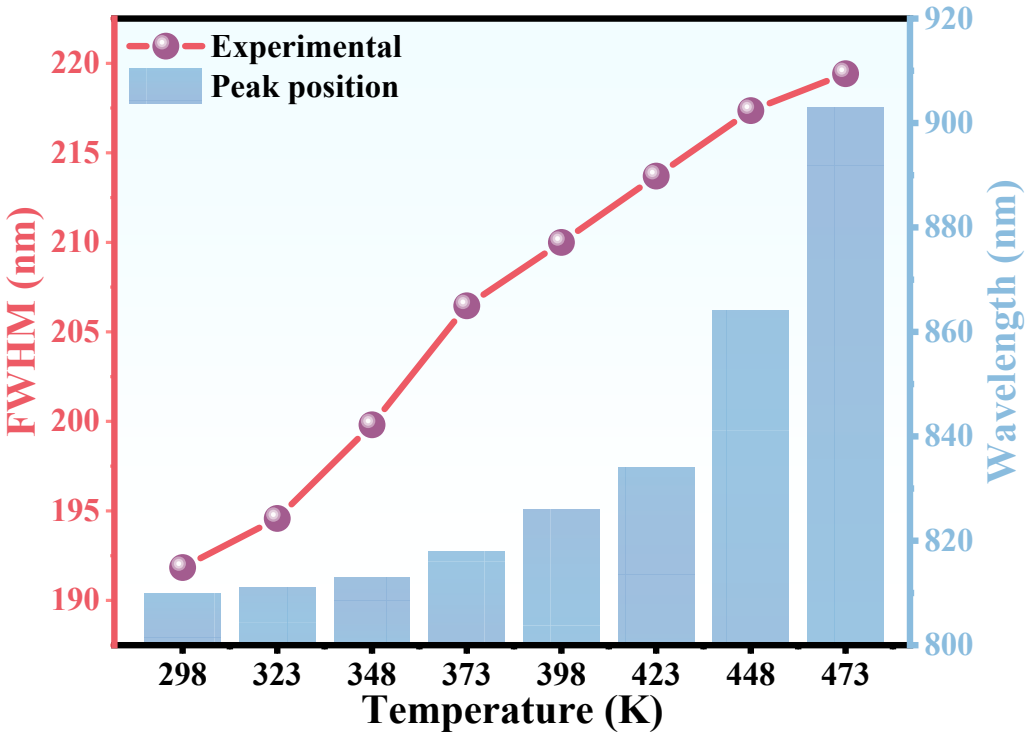

Figure S12. The FWHM and peak position of LZNO:0.01Cr^{3+},0.014Er^{3+} as a function of temperature.

As shown in Fig. S11, the continuous increase in temperature also led to changes in both emission peak position and band width of the spectrum. The peak position's redshift stems from a temperature-induced weakening of the crystal field environment, while the broadening of emission peak is due to the increasing amount of electrons excited at higher vibration levels with the increase of temperature[1-3]. Considering the strong electro-acoustic coupling effect and low thermal stability of Cr^{3+} in the LZNO system, corresponding activation energy (ΔE) of $LiZn_{0.986}Er_{0.014}NbO_4$:0.01$Cr^{3+}$ was obtained by means of equation(1):[4]

$$I_T = I_0\left[1 + cexp\left(-\frac{\Delta E}{kT}\right)\right]^{-1} \quad (1)$$

in which I_0 represents the initial emission intensity, I_T is the emission intensity of the phosphor at a certain temperature, c is a proportionality constant, k is Boltzmann constant (8.629×10^{-5} eV). Relational curve of $\ln[(I_0/I_T)-1]$~1/KT for the thermal quenching was plotted and fitted in Fig. S12, evidencing a lower ΔE value of 0.288 eV. The thermal quenching behavior can be expressed by the configuration coordinate diagram in Fig. S13.

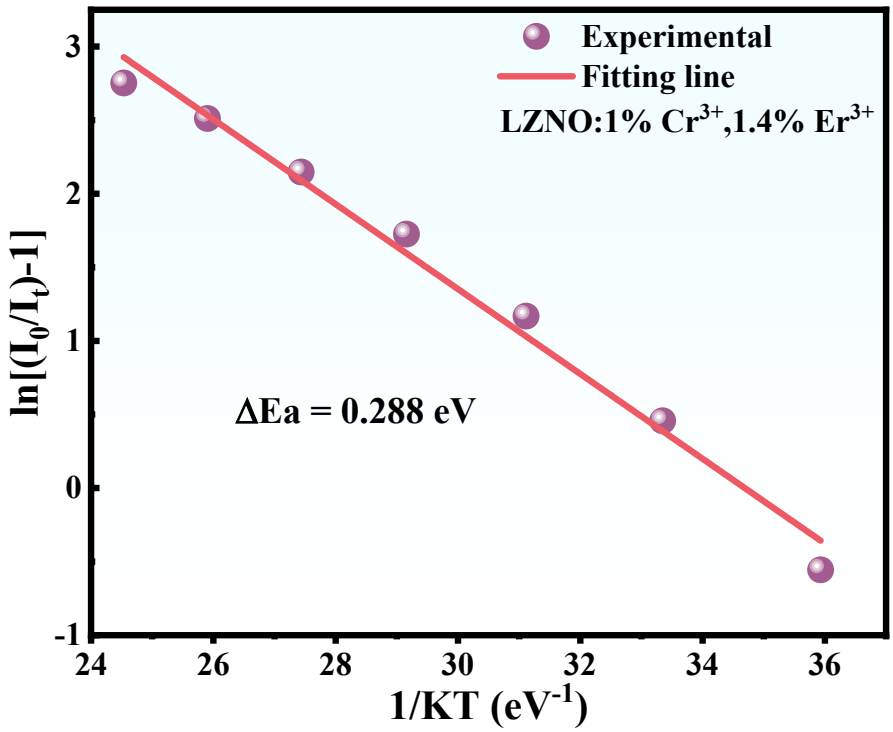

Figure S13. Relational curve of $\ln[(I_0/I_T)-1]\sim 1/TK$ for the thermal quenching in $LiZnNbO_4$:1%Cr^{3+},1.4%Er^{3+} phosphor.

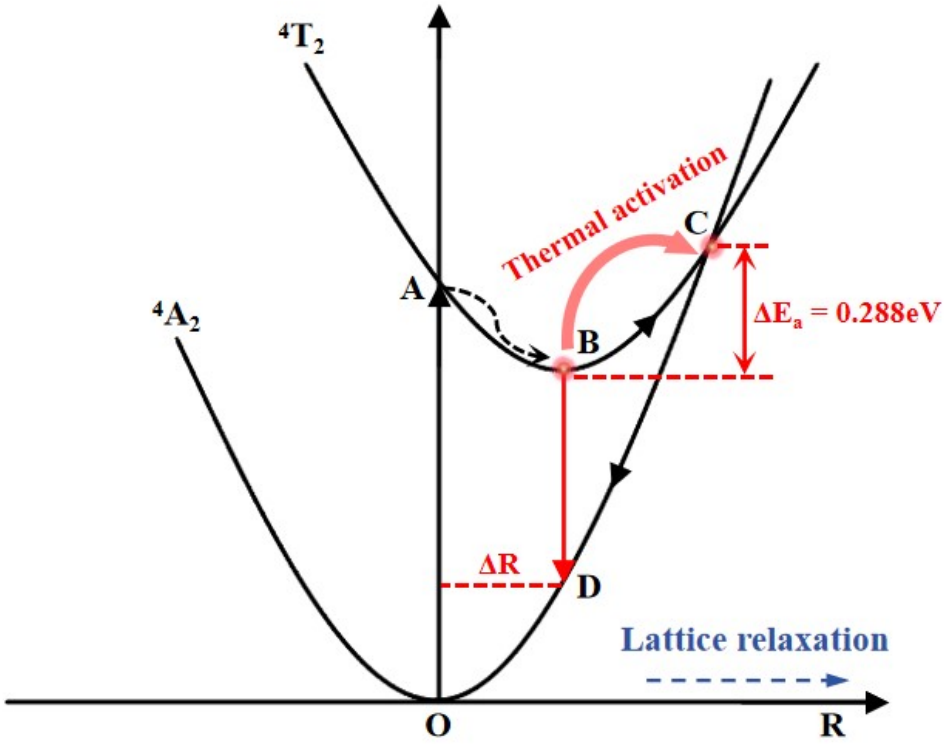

Figure S14. Configuration coordinate curves illustrating the thermal quenching of Cr^{3+} luminescence.

Paths O→A and B→D respectively represent the normal excitation and emission processes. The excited electrons are thermal activated by the elevated temperature to reach the intersection of the $^4T_2$ and $^4A_2$ curves (B→C) and then return to the $^4A_2$ ground state through nonradiative transition (C→O), leading to the so-called thermal quenching. The vertical height between point B and point C represents the activation energy (ΔEa) indicates the difficulty of this thermal activated process, which can be determined by the Arrhenius formula.

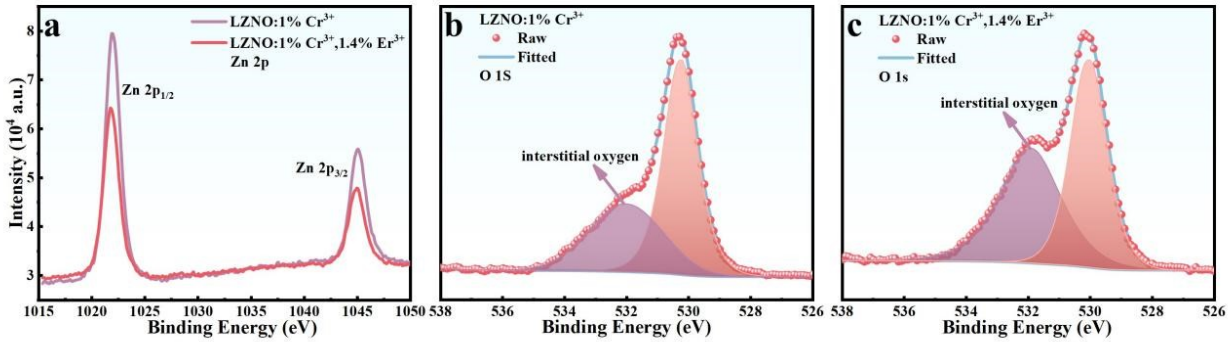

Figure S15. a) High-resolution Zn 2p XPS core energy level spectra of LZNO:0.01Cr^{3+} and LZNO:0.01Cr^{3+},0.014Er^{3+}. b) and (c) are high-resolution O 1s XPS core energy level spectras before and after Er^{3+} doping.

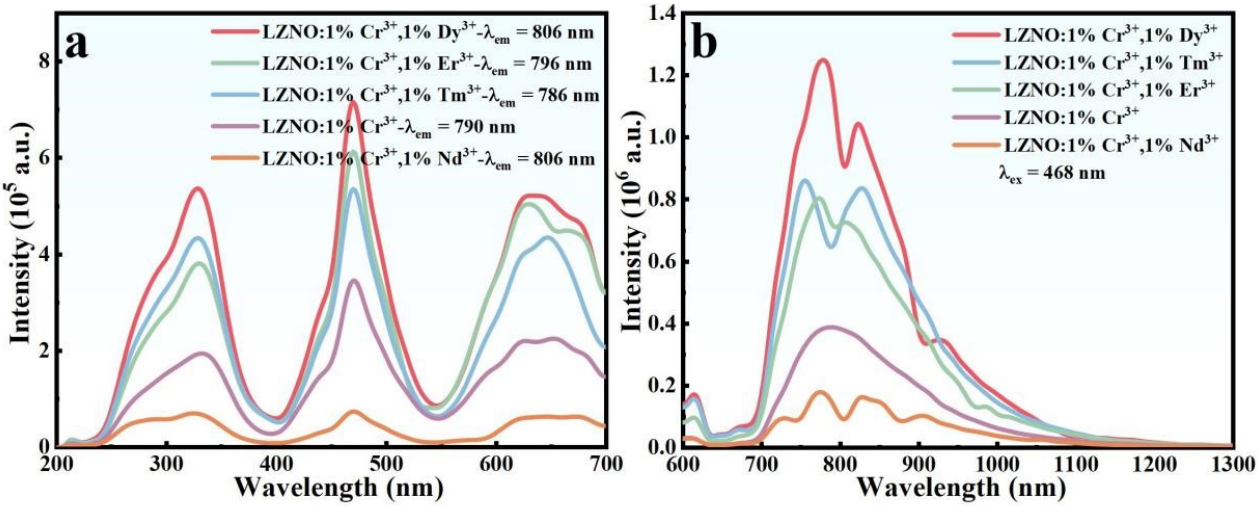

Figure S16. a) and (b) are PLE and PL were spectra of LZNO:0.01Cr^{3+} co-doped with different rare earth ions (Dy^{3+}, Tm^{3+}, Er^{3+} and Nd^{3+}).

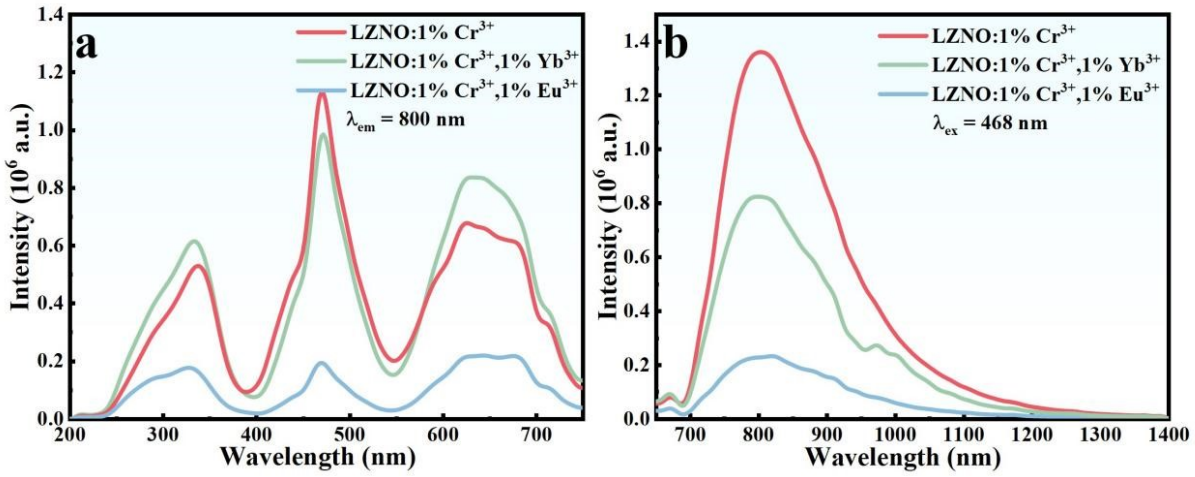

Figure S17. a) and (b) are PLE and PL were spectra of LZNO:0.01Cr^{3+} co-doped with Yb^{3+} and Eu^{3+}.

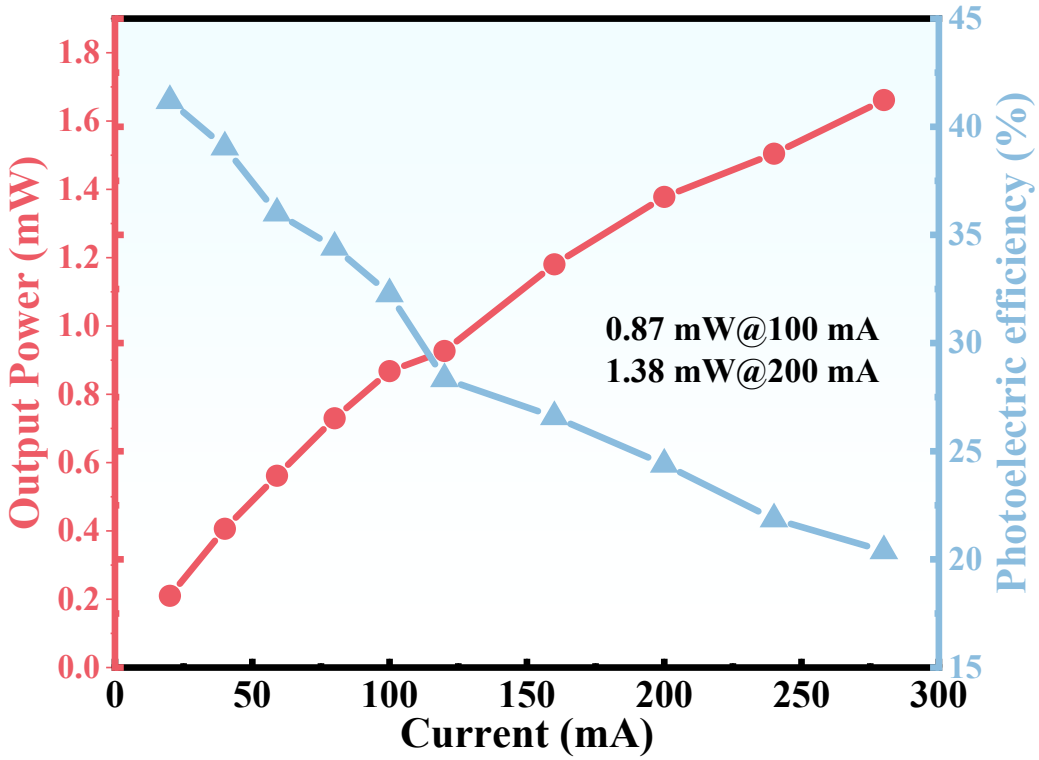

Figure S18. The output power and photoelectric conversion efficiency variation of NIR pc-LED with different currents.

Host	Spinel types	Excitation [nm]	Emission [nm]	Peak [nm]	FWHM [nm]
$ZnAl_2O_4$	Normal	531	640-780	686	-
$ZnGa_2O_4$	Normal	410	650-710	693	-
Zn_2SnO_4	Inverse	330	650-1200	800	170
$Zn_{1-x}Li_xGaO_4$	Normal	400	600-720	690	-
$ZnGa_2O_4$-Zn_2SnO_4	Normal-Inverse	254/435/550	600-950	700	-
$MgAl_2O_4$	Normal	395/430/550	600-780	687	-
$MgGa_2O_4$	Intermediate	420	650-900	705	50
Mg_2SnO_4	Inverse	467	600-1200	800	180
Mg_2TiO_4	Inverse	473	650-850	-	40
$Ga[Li_{0.5}Ga_{1.5}]O_4$	Inverse	420	650-850	715	-
Mg_2SnO_4-Zn_2TiO_4	Inverse-Inverse	470	650-850	754-720	129-48

Table S1. Spectroscopic properties of Cr^{3+}-activated spinel-type broadband NIR-I phosphor. (Full width at half maximum; FWHM).

	LZNO	LZNO:0.005Cr	LZNO:0.01Cr	LZNO:0.02Cr	LZNO:0.03Cr
Crystal	Tetragonal	Tetragonal	Tetragonal	Tetragonal	Tetragonal
Space group	$P4_122$	$P4_122$	$P4_122$	$P4_122$	$P4_122$
a/b, Å	6.0842(8)	6.0869(0)	6.0799(4)	6.0767(8)	6.0762(6)
c, Å	8.4048(6)	8.4096(9)	8.4006(5)	8.3985(7)	8.3997(3)
V, Å	311.1352(0)	311.5824(0)	310.5367(0)	310.1370(2)	310.1265(2)
R_{wp}%	9.104	9.839	9.268	9.517	8.936
χ^2	1.71	1.91	1.64	1.80	1.63

Table S2. Crystallographic parameters obtained from XRD Rietveld refinement of LZNO:xCr (x=0, 0.005, 0.01, 0.02, and 0.03), respectively.

	LZNO:0.01Cr,0.005Er	LZNO:0.01Cr,0.01Er	LZNO:0.01Cr,0.02Er
Crystal	Tetragonal	Tetragonal	Tetragonal
Space group	$P4_122$	$P4_122$	$P4_122$
a/b, Å	6.0854(2)	6.0774(9)	6.0862(4)
c, Å	8.4101(7)	8.3989(8)	8.4103(4)
V, Å	311.4481(7)	310.2248(3)	311.5395(2)
R_{wp}%	9.241	10.437	9.878
χ^2	1.75	2.13	1.93

Table S3. Crystallographic parameters obtained from XRD Rietveld refinement of LZNO:0.01Cr, xEr (x= 0.005, 0.01 and 0.02), respectively.

Atom	Wyck.	x	y	z	Uiso [Å^2]	n
Nb1	4b	0.2124(9)	0.5(0)	0.25(0)	0.0100	0.5
Zn1	4c	0.2588(0)	0.2588(0)	0.875(0)	0.0293	0.5
Li1	4a	0	0.2190(4)	0.5(0)	0.0269	0.5
O1	8d	-0.0035(1)	0.2493(9)	0.2240(5)	0.0321	1
O2	8d	0.2651(0)	0.5338(5)	0.4813(9)	0.0973	1

Table S4. Atomic coordinates and isotropic displacement parameters of LZNO.

References

1. X. Z. Chen, S. S. Liu, K. Huang, J. M. Nie, R. Kang, X. M. Tian, S. A. Zhang, Y. Li and J. R. Qiu, Cr^{4+} activated NIR-NIR multi-mode luminescent nanothermometer for double biological windows, *Chem. Eng. J.*, 2020, **396**, 6.
2. J. Y. Zhong, Y. Zhuo, F. Du, H. S. Zhang, W. R. Zhao and J. Brgoch, Efficient and Tunable Luminescence in $Ga_{2-x}In_xO_3:Cr^{3+}$ for Near-Infrared Imaging, *ACS Appl. Mater. Interfaces*, 2021, **13**, 31835-31842.
3. E. H. Song, H. Ming, Y. Y. Zhou, F. Q. He, J. C. Wu, Z. G. Xia and Q. Y. Zhang, Cr^{3+}-Doped Sc-Based Fluoride Enabling Highly Efficient Near Infrared Luminescence: A Case Study of $K_2NaScF_6:Cr^{3+}$, *Laser Photon. Rev.*, 2021, **15**, 8.
4. Y. Zhang, S. H. Miao, Y. J. Liang, C. Liang, D. X. Chen, X. H. Shan, K. N. Sun and X. J. Wang, Blue LED-pumped intense short-wave infrared luminescence based on Cr^{3+}-Yb^{3+}-co-doped phosphors, *Light-Sci. Appl.*, 2022, **11**, 12.